Journal of Power Sources 191 (2009) 448–455

Contents lists available at ScienceDirect

Journal of Power Sources

journal homepage: www.elsevier.com/locate/jpowsour

Influence of morphology on the behaviour of electrodes in a proton-conducting Solid Oxide Fuel Cell

R.T. Baker[a,*], R. Salar[b], A.R. Potter[c,1], I.S. Metcalfe[d], M. Sahibzada[e]

[a] School of Chemistry, University of St. Andrews, St. Andrews, Fife KY16 9ST, UK
[b] School of Chemical Engineering and Analytical Science, Manchester University, PO Box 88, Manchester M60 1QD, UK
[c] Division of Physical and Inorganic Chemistry, University of Dundee, Nethergate, Dundee DD1 4HN, UK
[d] University Research Centre in Catalysis and Intensified Processing, School of Chemical Engineering and Advanced Materials, Newcastle University, Newcastle upon Tyne NE1 7RU, UK
[e] Department of Materials, Imperial College, Exhibition Road, London SW7 2AZ, UK

ARTICLE INFO

Article history:
Received 2 December 2008
Received in revised form 4 February 2009
Accepted 14 February 2009
Available online 28 February 2009

Keywords:
Pt electrode
Impedance spectroscopy
Proton conductor
$SrCeO_3$
SOFC
Morphology

ABSTRACT

$SrCe_{0.95}Yb_{0.05}O_3$ (SCY) and related materials are under consideration as a proton conductors for Solid Oxide Fuel Cell (SOFC) electrolytes. Sintered pellets of SCY are used to perform impedance spectroscopy (IS) studies and fuel cell tests on cells with Pt electrodes of two different morphologies. Electrodes are applied to the SCY pellets by two routes: either by firing on a layer of Pt paint (denoted electrode P) or by magnetron sputtering (electrode S). In impedance spectra recorded over a wide temperature range under humidified hydrogen, in symmetrical cell conditions, cells with S electrodes give rise to a much smaller low frequency impedance feature than the cells with P electrodes. This is tentatively attributed to faster diffusion-related processes taking place at the S electrodes. The behaviour of working fuel cells with S and P electrode morphologies is evaluated in terms of maximum power output and Area Specific Resistance in two-atmosphere tests. The fuel cell anode with the S morphology results in superior fuel cell performance, in agreement with the impedance study. The influence of the two different electrode morphologies on the behaviour of the cells is discussed with reference to their morphology, as determined by SEM and AFM.

© 2009 Elsevier B.V. All rights reserved.

1. Introduction

Based on their chemical stability and electrical properties, $SrCe_{0.95}Yb_{0.05}O_3$ (SCY) and related compositions are under consideration as proton conductors for SOFC electrolytes [1–5]. The behaviour of an electrode in a fuel cell system is largely determined by its microstructure close to the interface with the electrolyte and the three phase boundary (TPB) [6,7]. Deposition of a finely divided layer of an electrode material in this region is likely to cause improvements in fuel cell performance, particularly if the material is catalytically active for the relevant half-reaction. In this study, platinum was chosen as the anode material because of its high temperature stability, excellent electrical conductivity and catalytic activity for the dissociation of H_2. Since it was desired to perform tests on a symmetrical cell as well as under fuel cell conditions, both electrodes of the cells were made of platinum. Two Pt electrode types with deliberately different morphologies were prepared on identical SCY electrolyte pellets. The effect of the difference in electrode morphology on the relevant electrochemical processes and on overall electrochemical performance was studied by impedance spectroscopy and in current–voltage and current–power measurements performed on operating fuel cells incorporating these electrodes. The morphology of the electrodes was examined using Scanning Electron Microscopy (SEM) and Atomic Force Microscopy (AFM).

2. Experimental

Fine $SrCe_{0.95}Yb_{0.05}O_3$ powder (Praxair Speciality Chemicals) of mean particle size, 0.7 μm, was uniaxially pressed into pellets and the pellets were fired in air at 1450 °C for 2 h. The fired pellets were 0.9 mm thick with a diameter of 19 mm. The densities of the fired pellets were estimated from their mass, geometric dimensions and the dimensions of the crystallographic unit cell [8]. Densities were found to be greater than 95% of the expected theoretical value. The XRD spectra of the starting powder and the fired pellets are given in Fig. 1. These were indexed to the $SrCe_{0.95}Yb_{0.05}O_3$ perovskite-like structure with space group, *Pmcn* (62) [8]. Peaks corresponding to

* Corresponding author. Tel.: +44 1334 463899; fax: +44 1334 463808.
E-mail address: rtb5@st-andrews.ac.uk (R.T. Baker).
[1] Now at ACAL Energy Ltd., Life Science Building, Crown Street, Liverpool L69 72B, UK.

0378-7753/$ – see front matter © 2009 Elsevier B.V. All rights reserved.
doi:10.1016/j.jpowsour.2009.02.039

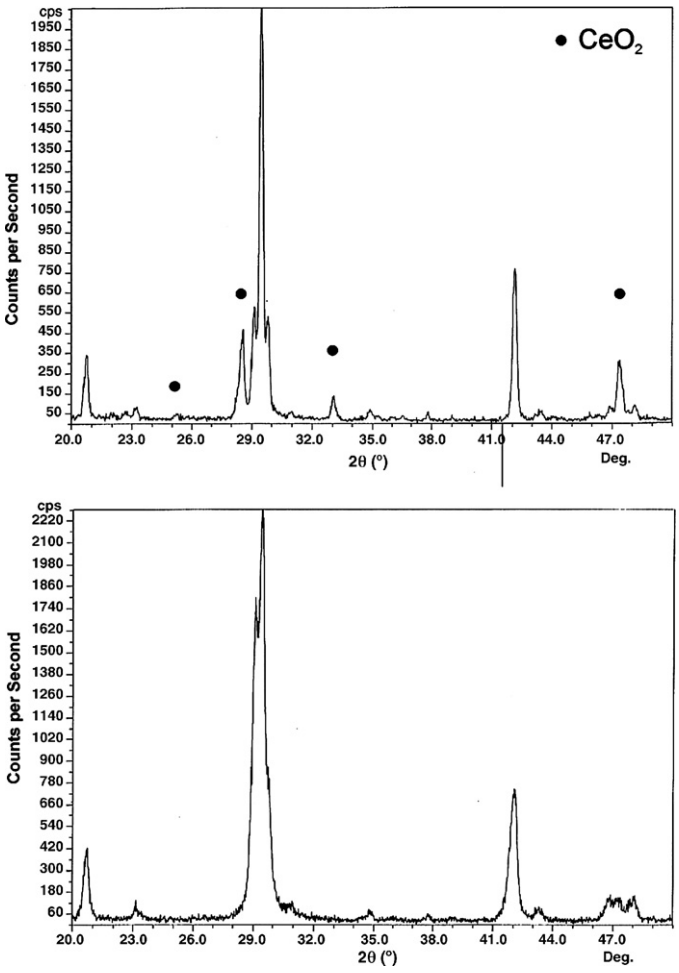

Fig. 1. XRD patterns for (a) the starting powder; (b) a sintered pellet of SCY. Peaks assigned to CeO_2 are indicated.

a small amount of CeO_2 [9] were detected in the powder but these were not seen in the case of the fired pellets. No peaks corresponding to SrO [10] were observed for either the powder or the fired pellet. Electrodes were applied to the faces of the electrolyte pellets by one of two methods. In the first method, inorganic-free Pt paint (Engelhard) was applied to the face of the electrolyte pellet and fired at 1000 °C. In the second method, the electrodes were applied by depositing a thin (*ca.* 1 μm) layer of Pt using a magnetron sputter coater (Cressington), over-painting this with the inorganic-free Pt paint and firing at 1000 °C. The two resulting electrode types will be denoted P (painted) and S (sputtered), respectively. Pt wire electrical contacts were attached to the electrodes by applying more Pt paint and re-firing.

In order to study the morphologies of the electrodes by SEM (Hitachi S-4700 FE-SEM and Philips XL30), layers of Pt were prepared on pellets of SCY to reproduce the electrolyte-electrode contact of the S and P electrodes by sputtering on a *ca.* 2 μm layer of Pt or by painting and firing on a single coating of Pt paint, respectively. The layers were not over-painted. Micrographs of the electrode layers were recorded in 'top–down' view in the SEM. The surface topology of the electrodes was measured using an Atomic Force Microscope (Digital Instruments). Cross-sectional SEM images of the used cells were also obtained by fracturing these after use in the electrochemical experiments, setting them in resin (Buehler) and polishing the exposed cross-sectional surface with successively finer diamond pastes (Buehler: 16 μm, 6 μm, 1 μm, 0.25 μm). Samples were carbon coated before examination in the SEM.

Impedance spectra were recorded using a Solartron 1260 Frequency Response Analyser over a temperature range of 100–820 °C. An AC potential difference of amplitude 100 mV was applied over a frequency range of 32 MHz to 0.01 Hz. For the impedance measurements, the cells were deployed in symmetrical cell mode, *i.e.* in a single-atmosphere apparatus with both electrodes exposed to the same gas composition. Both electrodes of each cell had the same morphology. That is, two types of cell were studied which had either two P electrodes or two S electrodes (henceforth denoted as the 2P and 2S cells, respectively). The sample cell under investigation was supported within a quartz reactor tube which was held in a vertical tube furnace (Leyton) equipped with a temperature programmer. The temperature of the sample was monitored using a thermocouple inserted into the reactor and positioned with its end slightly above the cell. Pt wires were used to make the electrical connections to the electrodes of the cell. The feed gas was pure hydrogen at one atmosphere and was humidified to 3% H_2O by passing it through a temperature-controlled water saturator before being supplied to the reactor along trace-heated lines at 250 ml min^{-1} (STP) using a mass flow controller. The composition of the outlet gas, particularly levels of O_2, N_2 and H_2O, was monitored using a quadrupole mass spectrometer (VG Micromass).

In separate experiments, the performance of fuel cells incorporating S and P electrodes was evaluated at 800 °C with humidified hydrogen fuel (3% H_2O saturation) fed to the anode and air at the cathode. All reactions were performed at atmospheric pressure. Four anode (A)–cathode (C) combinations were tested. These were denoted PA/PC (painted anode, painted cathode), PA/SC (painted anode, sputtered cathode), SA/SC (sputtered anode, sputtered cathode) and SA/PC (sputtered anode, painted cathode). In each case, the fuel cell was sealed onto the end of a 1/2-in. yttria-stabilised zirconia (YSZ) tube using a ceramic sealant, Autostic (Carlton Brown & Partners). The spent fuel gas from the anode was exhausted through a concentric 1/4 in. alumina tube. The outside electrode, *i.e.* the cathode, was exposed to air. The entire fuel cell assembly was placed inside a temperature controlled tubular furnace. The fuel gas was supplied at 50 ml min^{-1} (STP) and one atmosphere and a temperature-controlled saturator was used for humidification of the feed gas. The fuel cell exhaust passed through a heated line to a mass spectrometer and then to vent. Pt wires from the electrodes were connected to an external potentiostat/galvanostat to control the current and measure the voltage.

3. Results

3.1. Microstructural study

Micrographs obtained in the SEM of the two Pt layers taken in 'top down' view are presented in Fig. 2. At the lower magnifications the painted layer is seen to contain many large pores (Fig. 2(a)) whereas the sputtered coating is much more uniform (Fig. 2(b)). The pores in the painted layer can be seen to expose the surface of the electrolyte (Fig. 2(c)) while the sputtered layer is broken only by relatively narrow cracks (Fig. 2(d)). At high magnification, the painted metal appears to consist of large, highly dense crystals (of diameter 1–2 μm) whose terraced surfaces can be seen in Fig. 2(e) while the sputtered coating in Fig. 2(f) appears to be highly granular and porous with very small particles (of the order of 50 nm diameter). The topographic data obtained using the AFM are consistent with this. Images recorded for areas of dimensions 2 μm × 2 μm (Fig. 3(a and b)) and 10 μm × 10 μm (Fig. 3(c and d)) are presented. The large, relatively smooth particles of the painted layer (Fig. 3(a and c)), and

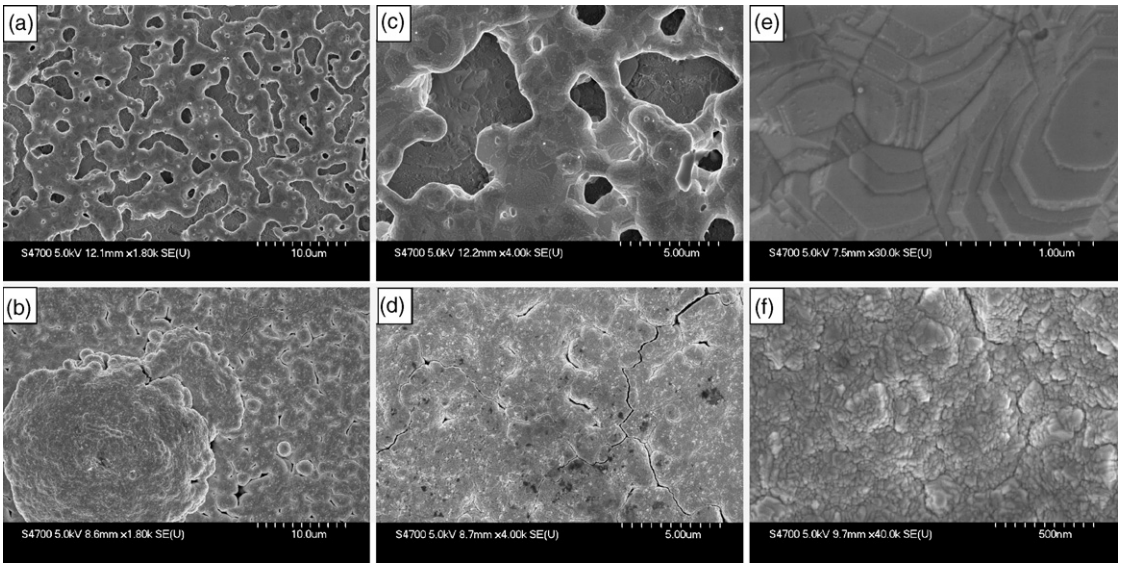

Fig. 2. SEM images showing the morphology of the two Pt electrode types. (a) Low magnification image of the P electrode showing numerous large pores; (b) low magnification image of the S electrode showing no large pores, only narrow cracks; (c) intermediate magnification image of P electrode showing that the pores extend down to the electrolyte surface and showing the dense nature of Pt between the pores; (d) intermediate magnification image of S electrode showing the relatively uniform coverage of the Pt layer and some of the cracks in this layer; (e) high magnification image of the P electrode in which the crystal terraces of the dense Pt material are evident; (f) high magnification image of the S electrode showing the small grain size and uniform nature of the Pt layer.

the rougher surface of the more granular sputtered layer (Fig. 3(b and d)) are both evident in the 3-D surface profiles. In addition, cross-sectional SEM images of the complete S and P electrodes after use in the electrochemical experiments were obtained by fracturing the cells, setting them in resin and polishing the exposed cross-sectional surface. A representative image of each is presented in Fig. 4. The P electrode consists of a painted electrode layer (PL) plus a similar, painted overlayer (O). These two layers cannot be distinguished and together are seen to be about 10 μm thick and to consist of mainly dense Pt material punctuated by pores which reach down to the SCY surface (Fig. 4(a)). The S electrode consists of the sputtered layer itself (SL) and a painted overlayer (O). The structure of fine pores, identified in the top–down SEM and AFM images of the sputtered layer, can be seen to extend throughout its thickness and length in Fig. 4(b) in contrast with the more dense microstructure of the painted overlayer. The total electrode thickness is similar to that of the P electrode.

3.2. Impedance spectroscopy study

Impedance spectroscopy measurements were made with the test cell operating in symmetric mode in a 3% humidified H_2 atmosphere. The spectra were fitted using the ZView software to an equivalent circuit model. This consisted of four sub-circuits connected to each other in series each of which consisted of a resistor and constant phase element in parallel. In order of decreasing characteristic frequency, these sub-circuits were assigned as relating to the bulk, grain boundary, charge transfer (ct) and electrode processes, respectively. It is often not possible to be certain about such assignments. However, care was taken to check assignments for consistency, for example by reference to the trends in characteristic frequency with changing temperature for each type of arc. In this work, charge transfer refers to loss or gain of electronic charge by electroactive atomic, molecular or ionic species at the three phase boundary and electrode processes include the adsorption, diffusion, desorption and reaction of electroactive species at the electrodes. Example spectra are given in Fig. 5(a–d) for the cell with P electrodes (top spectra) and the cell with S electrodes (lower spectra). Comparing the spectra for the two electrode types, it is clear that at high frequencies the spectra are very similar, implying very little change in the bulk and grain boundary conduction processes. This can be seen in the Arrhenius plot in Fig. 6 where bulk, grain boundary and total electrolyte (sum of bulk and grain boundary contributions) conductivity values for the 2S and 2P cells are very similar over a wide temperature range. That is, the difference in electrode morphology did not give rise to differences in the electrolyte response in the IS spectra. This is expected since the two electrolyte pellets were prepared in the same way. Apparent activation energies were estimated from the gradients of the best-fit lines to be 61 and 60 kJ mol^{-1} for bulk conductivity and 92 and 91 kJ mol^{-1} for grain boundary conductivity for the 2S and the 2P cells, respectively, the former being consistent with reported values for bulk protonic conductivity [3,4].

The arcs relating to the charge transfer and electrode processes are generally compounded. For the P electrode, the charge transfer response is of smaller resistance than the electrode response. Values of Area Specific Resistance (ASR, in Ωcm^2) were extracted in the case of the cell with P electrodes. For the S electrode, however, the charge transfer arc was measurable at very few temperatures because of its small size relative to the grain boundary and the electrode contributions in the spectra.

Very significant differences were observed in the lowest frequency feature, attributed to electrode processes, which was much larger for the 2P cell than for the 2S cell at all measurement temperatures. The implication of this is that the physicochemical processes at the electrodes giving rise to these features were much more efficient in the case of the sputtered electrode morphology than for the painted electrode.

Fig. 7 presents Arrhenius plots of the total ASR contribution extracted from the IS spectra for the electrolyte, for the charge transfer process (for the P electrode) and for the electrode process. For both electrode types, the electrolyte contribution dominated at the higher temperatures. However, for the 2P cell, the electrode ASR became important at low temperatures. This was not the case for the 2S cell whose electrode ASR was between half an order and nearly two orders of magnitude smaller than for the 2P cell. Activation energies for the ASR of the electrode process were estimated

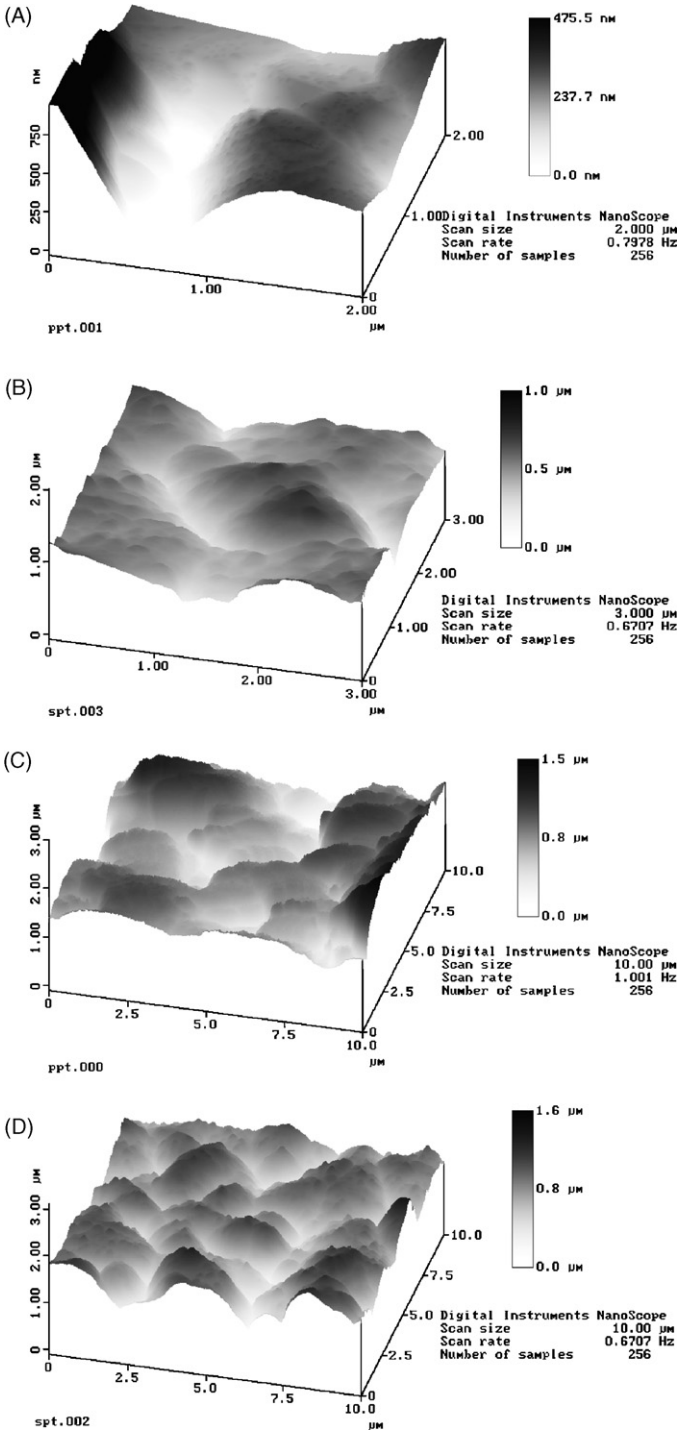

Fig. 3. Three dimensional representation of Atomic Force Microscope scans of (a) the typical smooth topology of the P type electrode over a 2 μm × 2 μm area; (b) typical granular topology of S type electrode over a 3 μm × 3 μm area; (c) topology of P type electrode over a 10 μm × 10 μm area; (d) topology of S type electrode over a 10 μm × 10 μm area. Gray levels indicate height of surface features.

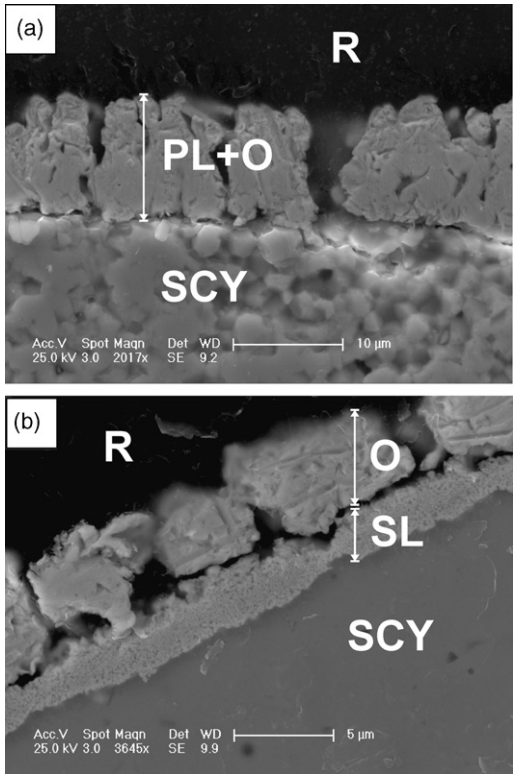

Fig. 4. SEM images of polished cross-sections showing (a) P electrode consisting of a painted layer and painted overlayer (PL + O) on SCY electrolyte, after use, and (b) S electrode consisting of the sputtered layer (SL) and painted overlayer (O), after use. Fracture and polishing has caused the SL and O to separate slightly and has left some polishing marks in the overlayer. The samples are embedded in resin (R).

from the plots to be 58 and 84 kJ mol^{-1} for the 2S and 2P cells, respectively.

The ASR of the charge transfer contribution to the spectra was extracted for the P electrode over a range of experimental temperatures. When plotted in Fig. 7 these present an approximately linear variation with inverse temperature. The apparent activation energy calculated from the gradient of the best-fit line is 78 kJ mol^{-1}.

3.3. Fuel cell tests

The effect of the two electrode types on the performance of four cell configurations – PA/PC, PA/SC, SA/PC, SA/SC – operated under fuel cell conditions at 800 °C was examined. The current–voltage and current–power characteristics obtained are shown in Fig. 8. The linear current–voltage relationship allowed an ohmic gradient, the ASR, to be extracted. Table 1 contains open circuit voltage (OCV), ASR and maximum power output (P_{max}) data for the four fuel cell configurations. The OCVs were found to be consistent with each other and only slightly below the theoretical value obtained from the Nernst equation of 1.05 V. This suggests both that the results for the four configurations were directly comparable and that leakage of gas between the cathode and anode atmospheres was negligible.

Table 1
Performance data for the four fuel cell configurations studied.

Fuel cell configuration	SA/SC	SA/PC	PA/SC	PA/PC
Anode preparation	Sputtered	Sputtered	Painted	Painted
Cathode preparation	Sputtered	Painted	Sputtered	Painted
Open circuit voltage, OCV (V)	1.00	1.02	1.00	1.02
Maximum power output (mW cm^{-2})	9.2	21.4	2.1	6.1
Area specific resistance (Ω cm^2)	18.1	12.1	123.5	40.7

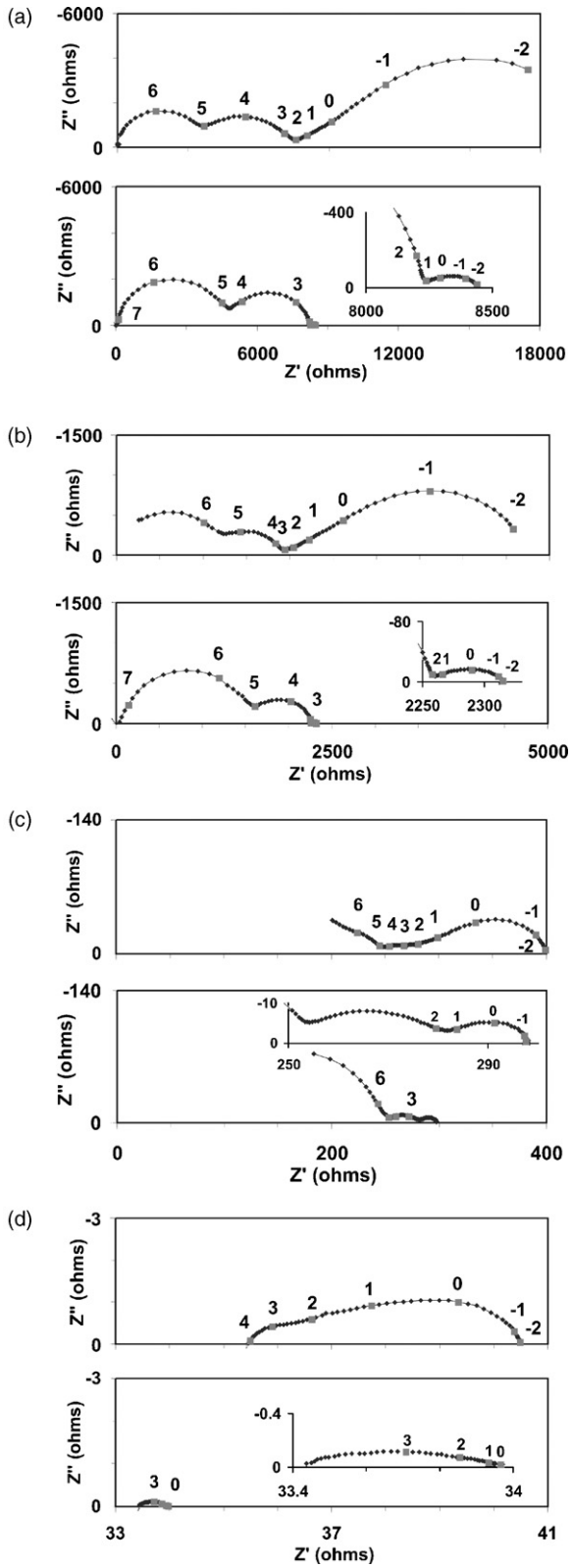

Fig. 5. Comparison of complex impedance spectra for cells with Painted (top) and Sputtered (and over-painted) (bottom) electrode configurations in 3% humidified hydrogen at (a) 245 °C; (b) 285 °C; (c) 380 °C; (d) 575 °C. Numerical labels indicate the common logarithm of the frequency of the applied potential.

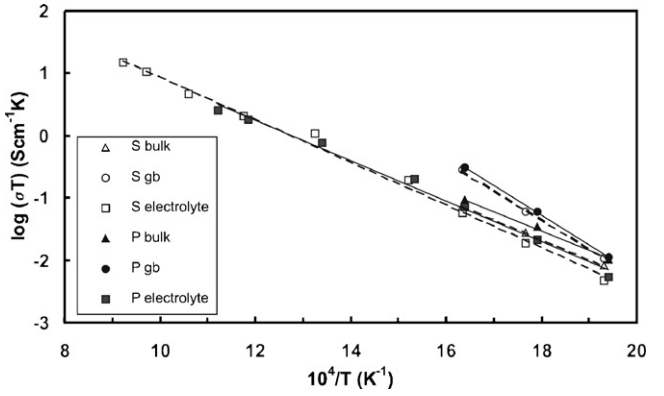

Fig. 6. Arrhenius-type plot for bulk, grain boundary (gb) and electrolyte conductivity (plotted as $\log(\sigma T)$) for cells with painted (P), and sputtered and over-painted (S), Pt electrodes. Data from impedance spectroscopy study (P: solid lines; S: dashed lines).

As shown in Fig. 8, there were very clear differences in performance between all of the different fuel cell configurations. The major finding here is that the S morphology always gives rise to considerably better performance than the P morphology when used at the anode. This is in agreement with the results of the impedance studies on the 2S and 2P cells, which were performed under anode conditions in a symmetrical cell configuration. Although the focus of this paper is on anode morphology, it is interesting to note from

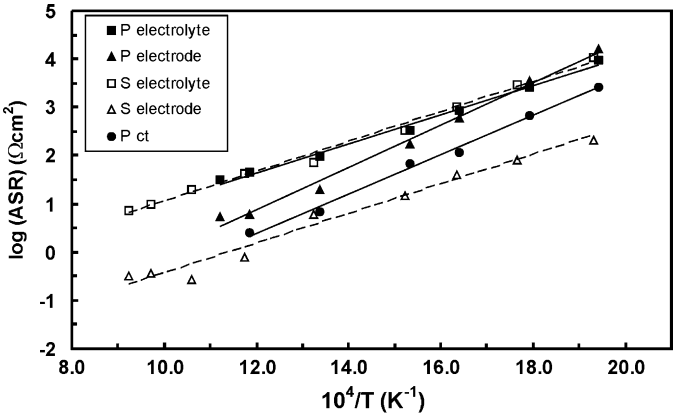

Fig. 7. Arrhenius plot of Area Specific Resistance (ASR) contribution of electrolyte, charge transfer (ct) and (non-charge transfer) electrode processes for cells with painted (P), and sputtered and over-painted (S), Pt electrodes. Data from impedance spectroscopy (P: solid lines; S: dashed lines).

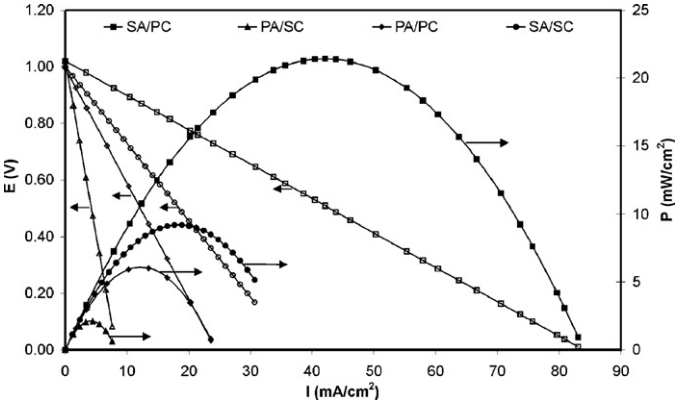

Fig. 8. Voltage–current and power–current data plots obtained at 800 °C in 3% humidified hydrogen for fuel cells with four different electrode configurations. In the legends, A = Anode; C = Cathode; S = Sputtered (and over-painted); P = Painted.

the results of the fuel cell tests that, for the cathode, the P morphology led to better cell performance than the S morphology. This behaviour was reproducible and implies that the S-type morphology is the more suitable for use at the anode while the P-type morphology is better for use at the cathode.

We note that the ASR for the best performing configuration, the SA/PC, was very similar to the expected performance based on the protonic conductivity of $SrCe_{0.95}Yb_{0.05}O_3$ reported in the literature. A conductivity of 0.006 S cm^{-1} at 800 °C for a symmetrical cell in hydrogen [1] would result in an ASR of about 14 Ω cm^2 for the 0.9 mm-thick pellet. This compares well with the measured result of 12.1 Ω cm^2. Bearing in mind that the value of conductivity will be affected to some extent by the defect concentration gradients across the fuel cell, this represents good agreement and indicates that the resistance associated with the electrodes for the SA/PC configuration was small. If we make the assumption that this latter resistance was negligible, we can apply the same calculation to the other results in order to estimate the combined electrode ASR in the fuel cell tests. We obtained values of about 4, 26 and 109 Ω cm^2 for the SA/SC, PA/PC and PA/SC configurations, respectively. These values provide a simple numerical comparison of the overall electrode performance in the four fuel cell configurations.

4. Discussion

In order to explain the variation of the features in the impedance spectra we have assigned as relating to charge transfer and electrode phenomena, and to explain the effect of anode morphology in the fuel cell tests, we must consider the processes taking place at the three phase boundary between electrode, electrolyte and gas, and on the surface of the Pt electrode material. At the high H_2 partial pressures used here, gas phase diffusion of hydrogen is unlikely to be a rate-limiting factor. Therefore, the processes to be considered are dissociative and non-dissociative adsorption of H_2, surface diffusion of H and H_2 species on the Pt to the TPB and the charge transfer reaction at the TPB itself. It is generally accepted that dissociative adsorption of H_2 on most metal surfaces, including that of Pt, is facile and has a low activation energy barrier [11]. Indeed, dissociative adsorption is often described as a non-activated process. Modelling [12] and other studies [6,11] show that very high coverages of hydrogen, of up to, and above, a ratio of one H atom per surface Pt, can be accommodated on Pt surfaces at low temperatures. However, there is strong evidence that as temperature is increased, the coverage of hydrogen falls very significantly. For example, in a Temperature Programmed Desorption (TPD) study, hydrogen coverages of up to 0.66 monolayers were established on a polycrystalline Pt foil [13]. In the spectra of the subsequent TPD experiments, three desorption peaks were identified but the rate of desorption fell to almost zero at about 190 °C, desorption having been essentially complete by this temperature. Therefore, we would expect hydrogen coverage to be low at the temperatures studied in the present work, and for coverage to decrease further with increasing temperature.

Kek et al. [14] performed D.C. polarisation studies on SCY-based electrochemical cells with electrodes of Ni, Ag, Au and Pt. Experiments were performed in dilute H_2 humidified with 0.7–1% water and over a temperature range of 600–850 °C. From these results the authors obtained apparent orders of the reaction at the hydrogen anode. For Ni this was close to one, suggesting the involvement of molecular H_2 in the rate determining step (rds), through either non-dissociative adsorption of H_2 or diffusion of molecular hydrogen on the surface of the metal. For Au, the apparent reaction order in H_2 was 0.5, indicating the involvement of atomic hydrogen in the rds. The authors cited dissociative adsorption of H_2, surface diffusion of atomic adsorbed species, H_{ads}, or reaction of H_{ads} in the charge transfer step as possibilities. Finally, for the Ag and Pt electrodes, an intermediate reaction order of 0.75 was obtained. The authors suggest that a high (>0.01) hydrogen coverage may have masked the true reaction order. However, their other results for Pt suggested complex behaviour that could indicate that two parallel electrode processes were taking place under the conditions employed. Kek and Bonanos [15] performed a study on proton conducting cells based on SCY in 1–10% H_2 at 600–800 °C. They extracted empirical activation energies for the electrode process. From the resistance associated with the low frequency arc in impedance spectra they obtained values of 79 kJ mol^{-1} for a Ni electrode and 90 kJ mol^{-1} for an Ag electrode. The resistance values used to obtain these activation energies related to the overall electrode process. That is, the charge transfer contribution was not isolated from the low frequency electrode process. DC polarisation data obtained in the same study gave values of 68 and 106 kJ mol^{-1} for Ni and Ag, respectively. These compared with a previous value obtained using a porous Pt electrode of 50 kJ mol^{-1} [16]. Jiang and Badwal [17] studied the hydrogen oxidation reaction at the anode of a working yttria-stabilised zirconia-based fuel cell with painted Pt electrodes using D.C. polarisation measurements and impedance spectroscopy. For Pt in dry and humidified hydrogen at 1000 °C, two strongly overlapping impedance arcs were obtained. In decreasing order of characteristic frequency, these were attributed to the charge transfer process, taking place at the TPB, and an electrode process involving adsorption and surface diffusion of hydrogen. The P electrode used in the present study had very similar morphology to that of the cited study by Jiang and Badwal [17], both having been prepared by painting and firing. Therefore, applying the same arguments to the present study, at least for the P electrode at high temperatures, we might expect that the overall anode reaction would be dependent upon the coverage of the electroactive hydrogen species at the TPB at higher characteristic frequencies (shorter time constants) and on the adsorption and subsequent diffusion of surface hydrogen species to the TPB at lower characteristic frequencies (longer time constants). In our work, we both varied the morphology of the electrode and recorded spectra over a wide range of temperatures. The charge transfer ASR for the P electrode showed approximately linear dependence on inverse temperature over the whole temperature range investigated (Fig. 7) and had an apparent activation energy of 78 kJ mol^{-1}. This suggests that there was no dramatic change in the nature of the corresponding physicochemical process with changing temperature. This process is likely to be governed both by the temperature-dependence of the availability of hydrogen species at the TPB and by the rate of the actual charge transfer reaction in which the hydrogen species adsorbed at the TPB are transferred to the SCY and lose electrons to the electrode. This latter process is closely related to spillover in heterogeneous catalysis. This is particularly relevant in light of (i) the importance of water absorption by SCY in the mechanism of proton conduction [5], (ii) the possibility of forming surface hydroxyl species on CeO_2 surfaces by spillover from, for example, Rh in Rh/CeO_2 catalysts [18] and (iii) considering the high surface electronic conductivity of Ce-based oxides. Spillover has been reported to be the rds in adsorption of hydrogen onto supported metal catalysts, and was estimated to have an activation energy of 35.5 kJ mol^{-1} in a Pt/WO_3-ZrO_2 catalyst [19] (although activation energy is likely to be a strong function of composition of the support material).

In light of the above discussion, it is likely, on balance, that the process responsible for the low frequency feature in the IS spectra relates to the combined adsorption and surface diffusion of hydrogen species to the TPB [7,8,17]. This process is likely to be less efficient (*i.e.* more resistive in the IS spectrum) for the large, low specific surface area Pt particles which characterise the P electrode morphology than for a granular layer of much

smaller, higher specific surface area particles observed in the case of the S electrode (compare Fig. 2(e and f)). In the S electrode, the much smaller average Pt particle size implies both that the surface of the Pt electrode can accommodate more adsorbed H species (in terms of total moles of hydrogen adsorbed, rather than surface coverage) and that the average distance an adsorbed species must diffuse across the Pt surface to reach the TPB (the mean path length) is much shorter than for the P electrode. For these reasons, the S electrode would be expected to present lower ASR associated with the low frequency electrode arc. Our low frequency impedance results can thus be explained in terms of the different electrode morphologies, as observed by SEM and AFM.

The values of overall activation energies derived in the present work are broadly consistent with values obtained in the previous studies discussed above. However, the apparent activation energies for the electrode process with the P and the S morphology were different from each other, at 84 and 58 kJ mol^{-1}, respectively. This may be due to the electrode ASR having a complex dependence on a number of contributing processes (as suggested above [14]), the balance of these processes being determined by the different electrode morphologies. It is interesting that diffusion of adsorbed molecular H_2 on Pt electrodes has been proposed in connection with an activation energy of 50 kJ mol^{-1} [8], not far from the 58 kJ mol^{-1} estimated here for the S electrode. Surface diffusion of $H_{(ads)}$ is reported to have a lower activation energy of about 20 kJ mol^{-1} [12]. However, according to Weinberg and Merrill [20], the potential wells for adsorbed hydrogen species on a Pt(1 1 1) surface are such that the activation energy barrier to conversion of molecularly adsorbed $H_{2(ads)}$ to atomically adsorbed $H_{(ads)}$ is about 58 kJ mol^{-1} while the reverse process has a barrier of 113 kJ mol^{-1} and conversion of chemisorbed $H_{2(ads)}$ to physisorbed, or 'pre-cursor', $H_{2(ads)}$ has an activation barrier of 71 kJ mol^{-1}. The ASR of the low frequency electrode feature could be dependent on a combination of contributions from sub-surface diffusion, adsorption, conversion of $H_{2(ads)}$ into $H_{(ads)}$ as well as surface diffusion, possibly involving one of the latter processes, the ratio of the contributions changing with changing electrode morphology. For the S electrode, the conversion of $H_{2(ads)}$ to $H_{(ads)}$, during the adsorption/diffusion process, may be the rds. It could be envisaged that the major mechanism of surface diffusion of hydrogen (via $H_{2(ads)}$ or $H_{(ads)}$, for example) is sensitive to the mean path length of diffusion to the TPB, this being determined by the morphology of the electrode, and so being different for the P morphology. However, caution is required when analysing the origin of such activation energies as these are overall activation energies and are therefore difficult to assign to identifiable processes. Furthermore, all of these processes are likely to be strongly influenced by the nature of the Pt surface. The nature of the surface planes, surface defect, step and edge concentrations are all known to have a strong effect on adsorption and diffusion on Pt and other metals [21]. Therefore, further work would be required to draw firmer conclusions from the values of activation energies obtained here.

The major finding of the fuel cell experiments is that the S electrode morphology at the anode is the most favourable, in agreement with the IS results and the above discussion. However, although this work is focussed on the fuel cell anode, it is interesting to briefly consider the effect of the morphology of the cathode in the fuel cell results, which was the opposite of that observed for the anode. The best cell performance was observed when the coarser morphology of the P electrode was employed as the cathode. The P electrode is characterised by large, dense particles of Pt which form a matrix with relatively large pores. In the SEM images (Fig. 2) these pores are seen to reach down to the electrolyte surface. Oxygen adsorption on Pt surfaces is not a very favoured process [17]. Diffusion of O on Pt is also slow and was suggested as the rds for the electrode process at the Pt cathode in a polarisation study of a Pt/SCY/Pt cell [22]. On the contrary, the electronic and ionic conductivity of the surfaces of Ce-based oxides can be very high, particularly when the oxide is reduced and so contains Ce^{3+} and oxygen vacancy sites. On Pt/CeO_2 catalysts [23], adsorption of oxygen on Pt, and on the oxide, was found to be a slow process while spillover of oxygen onto the CeO_2 support and surface diffusion of oxygen on the support and on Pt were found to be faster processes. Fast surface diffusion of oxygen over distances of 1 μm on CeO_2 was considered reasonable at a temperature of 400 °C [20], and the fuel cell tests presented here were performed at 800 °C. Therefore, it seems that our results on the superiority of the P over the S type cathode morphology could be attributed to the formation of a cathodic reaction zone on the SCY surface extending out from the TPB, perhaps by several micrometers. The pores in the P electrode are of diameters of about 1–10 μm, so that, at our fuel cell operating temperature of 800 °C, most of the electrolyte surface area exposed may be actively involved in the cathode reaction. Hence, in one sense, the nature and existence of these pores in the Pt cathode structure would be more important than the nature of the surrounding Pt.

5. Conclusions

Pt electrodes with two deliberately very different morphologies were prepared. Magnetron sputtering gave rise to Pt electrodes of a finely divided, granular and uniform morphology with grains of about 50 nm diameter (S electrode). Painting gave rise to a denser Pt matrix which consisted of μm-scale crystals and was punctuated by large pores (P electrode).

In impedance spectroscopy studies performed on symmetrical cells under humidified hydrogen, the finely divided electrode morphology obtained by sputtering gave rise to a significantly smaller low frequency feature in the impedance spectra than did the painted electrode morphology. This feature was ascribed to diffusion-related processes occurring on the Pt electrode surface in the vicinity of the TPB. These processes appear to have been much more rapid in the case of the morphology obtained by sputtering than that obtained by painting. The apparent activation energy relating to this process was also lower for the sputtered electrode morphology.

At slightly higher frequencies in the impedance spectra, the feature ascribed to the charge transfer process was also quantified for the P electrode and had an apparent activation energy of 78 kJ mol^{-1}.

Fuel cell tests were performed on cells incorporating S and P electrodes in four different configurations using a humidified hydrogen fuel at the anode and air at the cathode. Performance was assessed in terms of maximum power output and ASR. Importantly, and in agreement with the impedance spectroscopy results, the S morphology was clearly superior to the P morphology for use at the anode.

The possible physical origins of the effect of anode morphology on the electrode and charge transfer responses in the impedance spectra and on the performance of fuel cells with anodes of these morphologies are discussed in detail.

A further finding of interest in the fuel cell tests was that while the P morphology results in a poor anode, it is the more suitable morphology for use at the cathode. The possible role of the electrolyte surface exposed by the pores in the painted cathode as an extended cathodic reaction zone is discussed briefly.

The ASR of the best performing fuel cell configuration (SA/PC) was similar to that expected from consideration of the conductivity of the electrolyte alone, indicating that the resistance of the electrodes was small in this case.

Acknowledgements

This work was funded by the EPSRC (grants GR/N05604 and GR/N06458). M.S. acknowledges the award of a Royal Academy of Engineering research fellowship. R.T.B. thanks Dr. Alan Prescott and Dr. Yongchang Fan for their assistance with SEM and AFM characterisation, respectively.

References

[1] H. Iwahara, T. Esaka, H. Uchida, N. Maeda, Solid State Ionics 3–4 (1981) 359.
[2] H. Iwahara, in: P. Colomban (Ed.), Proton Conductors, Cambridge University Press, 1992, p. 511.
[3] T. Scherban, W.-K. Lee, A.S. Nowick, Solid State Ionics 28–30 (1988) 585.
[4] E.O. Ahlgren, J.R. Hansen, N. Bonanos, F.W. Poulsen, M. Mogensen, Proc. 17th Risø Int. Symp. Mater. Sci., 1996, p. 161.
[5] N. Bonanos Philips, F.W. Poulsen, E.O. Ahlgren, Solid State Ionics 125 (1999) 389.
[6] J. Mizusaki, H. Tagawa, K. Isobe, M. Tajika, I. Koshiro, H. Maruyama, K. Hirano, J. Electrochem. Soc. 141 (6) (1994) 1674.
[7] N. Bonanos, Proc. 14th Int. Risø Symp. on Mater. Sci., 1993, p. 19.
[8] K.S. Knight, N. Bonanos, Mater. Res. Bull. 30 (3) (1995) 347–356.
[9] E.A. Kuemmerle, G. Heger, J. Solid State Chem. 147 (1999) 485–500.
[10] W. Primak, H. Kaufman, R. Ward, J.A.C.S 70 (1948) 2043–2046.
[11] V. Ponec, G.C. Bond, Catalysis by metals and alloys, in: Studies in Surface Science and Catalysis, vol. 95, Elsevier, 1995, pp. 356–436.
[12] P. Légaré, Surf. Sci. 559 (2–3) (2004) 169.
[13] V.D. Thomas, J.W. Schwank, J.D. Gland, Surf. Sci. 501 (3) (2002) 214.
[14] D. Kek, N. Bonanos, M. Mogensen, S. Pejovnik, Solid State Ionics 131 (2000) 249.
[15] D. Kek, N. Bonanos, Solid State Ionics 125 (1999) 345.
[16] H. Uchida, H. Kimura, H. Iwahara, J. Appl. Electrochem. 20 (1990) 390.
[17] S.P. Jiang, S.P.S. Badwal, J. Electrochem. Soc. 144 (1997) 3777.
[18] S. Bernal, J.J. Calvino, G.A. Cifredo, A. Laachir, V. Perichon, J.M. Herrmann, Langmuir 10 (1994) 717.
[19] S. Triwahyono, T. Yamada, H. Hattori, Appl. Catal. A 250 (1) (2003) 65.
[20] W.H. Weinberg, R.P. Merrill, Surf. Sci. 33 (1972) 493.
[21] K. Christmann, Surf. Sci. Rep. 9 (1988) 1.
[22] H. Uchida, S. Tanaka, H. Iwahara, J. Appl. Electrochem. 15 (1985) 93.
[23] A. Holmgren, D. Duprez, B. Andersson, J. Catal. 182 (1999) 441.